REPORT

NANOPHOTONICS

Determining plasmonic hot-carrier energy distributions via single-molecule transport measurements

Harsha Reddy[1]*, Kun Wang[2]*, Zhaxylyk Kudyshev[1,3], Linxiao Zhu[2], Shen Yan[2], Andrea Vezzoli[4], Simon J. Higgins[4], Vikram Gavini[2,5], Alexandra Boltasseva[1], Pramod Reddy[2,5]†, Vladimir M. Shalaev[1]†, Edgar Meyhofer[2]†

Hot carriers in plasmonic nanostructures, generated via plasmon decay, play key roles in applications such as photocatalysis and in photodetectors that circumvent bandgap limitations. However, direct experimental quantification of steady-state energy distributions of hot carriers in nanostructures has so far been lacking. We present transport measurements from single-molecule junctions, created by trapping suitably chosen single molecules between an ultrathin gold film supporting surface plasmon polaritons and a scanning probe tip, that can provide quantification of plasmonic hot-carrier distributions. Our results show that Landau damping is the dominant physical mechanism of hot-carrier generation in nanoscale systems with strong confinement. The technique developed in this work will enable quantification of plasmonic hot-carrier distributions in nanophotonic and plasmonic devices.

Hot carriers, which are energetic electrons and holes with energy distributions that deviate substantially from equilibrium Fermi-Dirac distributions (*1*), are expected to arise in metallic nanostructures because of the nonradiative decay of surface plasmons. Such hot carriers hold promise for the development of a variety of technologies, including plasmon-driven photochemistry (*2*–*5*), alternative solar energy harvesting devices (*6*), and efficient photodetectors operating below bandgap (*7*–*9*). Central to the design and development of these applications is knowledge of the hot-carrier energy distributions (HCEDs) that are generated under steady-state conditions (*10*). Although previous work has tried to quantify HCEDs (*11*–*15*), most of it has relied on first-principle calculations or semiclassical approaches, which involve assumptions about the dominant relaxation pathways of hot carriers as well as material properties (*15*) that lead to considerable uncertainties in the estimated HCEDs (*12*, *13*). In fact, recent calculations (*16*) have even suggested that the deviations from the equilibrium Fermi-Dirac distribution are negligibly small, calling past calculations into question. Therefore, direct experimental observations are critical for obtaining detailed insights into the HCEDs and for rationally engineering the aforementioned technologies.

Here, we show how scanning probe–based techniques (*17*–*19*) that measure charge transport in single molecules, when combined with nanoplasmonic experimental methods, can be leveraged to directly quantify steady-state HCEDs [$f_{hot}(E)$] in a key model system—a thin gold (Au) film that supports propagating surface plasmon polaritons (SPPs). Our basic strategy is to first create single-molecule junctions (SMJs)—using carefully chosen molecules with appropriate transmission characteristics—between a plasmonic Au film and the Au tip of a scanning tunneling microscope (STM) and then elucidate the current-voltage characteristics with and without plasmonic excitation at various voltage biases (V_{bias}) (see Fig. 1A). The difference in the measured currents for the cases with [$I_{SPP}(V_{bias})$] and without [$I_d(V_{bias})$] plasmonic excitation, which we call the hot-carrier current $I_{hot}(V_{bias}) = I_{SPP}(V_{bias}) - I_d(V_{bias})$, enables us to directly quantify $f_{hot}(E)$.

As depicted in Fig. 1, B and C, $I_{hot}(V_{bias})$ arises because of the generation of the nonequilibrium carriers under plasmonic excitation with an energy distribution $f_{ne}(E)$. We note that the energy distribution $f_{hot}(E)$ represents the difference between $f_{ne}(E)$ and the equilibrium Fermi-Dirac distribution $f_{eq}(E)$ as $f_{hot}(E) = f_{ne}(E) - f_{eq}(E)$. As explained in detail in the supplementary materials (*20*), $f_{hot}(E)$ and $I_{hot}(V_{bias})$ are related by

$$I_{hot}(V_{bias}) = \frac{2e}{h}\int_{-\infty}^{\infty} T(E)\, f_{hot}\left(E - \frac{eV_{bias}}{2}\right) dE \qquad (1)$$

where $T(E)$ is the transmission function of the SMJ, e is the elementary charge, and h is the Planck constant. When SMJs that feature a sharp peak in $T(E)$ are used, $I_{hot}(V_{bias})$ is predominantly determined by the hot carriers with energies close to the transmission peak, simplifying the above integral to [(*20*), section 1]

$$I_{hot}(V_{bias}) \approx \frac{2e}{h} f_{hot}\left(E_0 - \frac{eV_{bias}}{2}\right)\int_{-\infty}^{\infty} T(E)\, dE \qquad (2)$$

where E_0 is the energy of the peak in $T(E)$. Equation 2 relates $I_{hot}(V_{bias})$ to $f_{hot}(E)$ via a voltage- and energy-independent constant scaling factor $\left[\frac{2e}{h}\int_{-\infty}^{\infty} T(E)dE\right]$. Therefore, by varying V_{bias} in the window $\{V_0{:}-V_0\}$, the steady-state HCEDs can be mapped within the energy window $\left\{E_0 - \frac{eV_0}{2} : E_0 + \frac{eV_0}{2}\right\}$ (Fig. 1C).

We used the molecules shown in Fig. 1D (labeled **L1**, **H1**, and **L2**) for experimental quantification of the HCEDs. Molecule **L1** represents a charge-transfer complex of quaterthiophene (T4) and tetracyanoethylene (TCNE) with terminal thiophenes containing gold-binding methyl sulfides, while the **H1** molecule, 3,4-ethylenedioxythiophene (EDOT), is flanked by two thiophenes with terminal thiophenes containing gold-binding methyl sulfides. The transmission characteristics of Au-**L1**-Au and Au-**H1**-Au SMJs are expected to be sharply peaked and dominated by the lowest unoccupied molecular orbital (LUMO) (*21*, *22*) and highest occupied molecular orbital (HOMO) (*23*), respectively. We also used **L2** molecules, 1,4-benzenediisonitrile [see (*20*), section 3, for additional details]; SMJs created from **L2** are expected to feature weakly energy-dependent $T(E)$ also dominated by the LUMO level (*24*).

Plasmonic gold films (thickness: 6 and 13 nm), with integrated grating couplers, were fabricated on fused silica substrates (Fig. 1A) to excite SPPs and generate hot carriers [(*20*), section 4]. The 6-nm-thick gold film with a grating coupler was first exposed to a solution containing **L1** molecules to create a monolayer of the molecules [(*20*), section 5]. Next, we positioned a Au STM tip at a separation of ~1 μm (along the x direction) from the grating edge (fig. S2). Subsequently, the Au film was covered with an immersion oil matching the refractive index of fused silica to create a symmetric optical medium around the film, and a V_{bias} of 0.1 V was applied to the STM tip while grounding the Au film. We then used the STM break junction technique (*17*, *18*) [see (*20*), section 2, for a detailed protocol] to identify the current through a Au-**L1**-Au SMJ. The peak in the current histogram created from more than 2000 current versus displacement traces represents the most probable current (I_d)—corresponding to a conductance of 8.5×10^{-4} G_0 for a

[1]School of Electrical and Computer Engineering, Purdue University, West Lafayette, IN 47907, USA. [2]Department of Mechanical Engineering, University of Michigan, Ann Arbor, MI 48109, USA. [3]Center for Science of Information, Purdue University, West Lafayette, IN 47907, USA. [4]Department of Chemistry, University of Liverpool, Liverpool L69 7ZD, UK. [5]Department of Materials Science and Engineering, University of Michigan, Ann Arbor, MI 48109, USA.
*These authors contributed equally to this work.
†Corresponding author. Email: pramodr@umich.edu (P.R.); shalaev@purdue.edu (V.M.S.); meyhofer@umich.edu (E.M.)

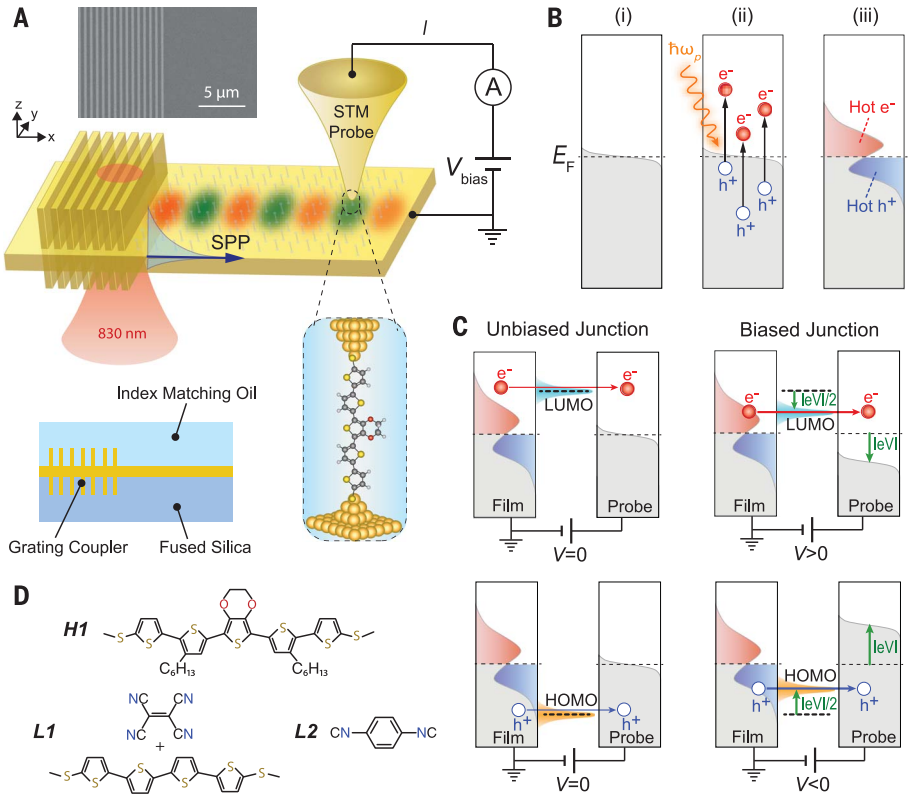

Fig. 1. Experimental setup and strategy to map hot-carrier energy distributions (HCEDs). (**A**) Schematic of the experimental setup. SMJs are formed between a grounded nanodevice (Au film with integrated grating coupler; see electron micrograph inset) and a biased Au STM probe. SPPs are excited by illuminating the grating coupler with an 830-nm continuous wave laser. *I*, current; Ⓐ, ammeter. The bottom-left graphic represents a cross section of the nanodevice covered with index-matching oil. (**B**) Schematic of hot-carrier generation. (i) Equilibrium Fermi function. (ii) Nonradiative decay of SPP energy ($\hbar\omega_p$) generates electron-hole pairs, resulting in (iii) nonequilibrium distribution of hot electrons and holes. (**C**) Schematic showing how LUMO- or HOMO-dominated SMJs with sharp transmission peaks selectively transmit hot carriers. Biasing the junctions shifts the transmission peak with respect to the equilibrium Fermi level, enabling quantification of HCED. (**D**) Structures of the three molecules (**H1**, **L1**, and **L2**) used in this work.

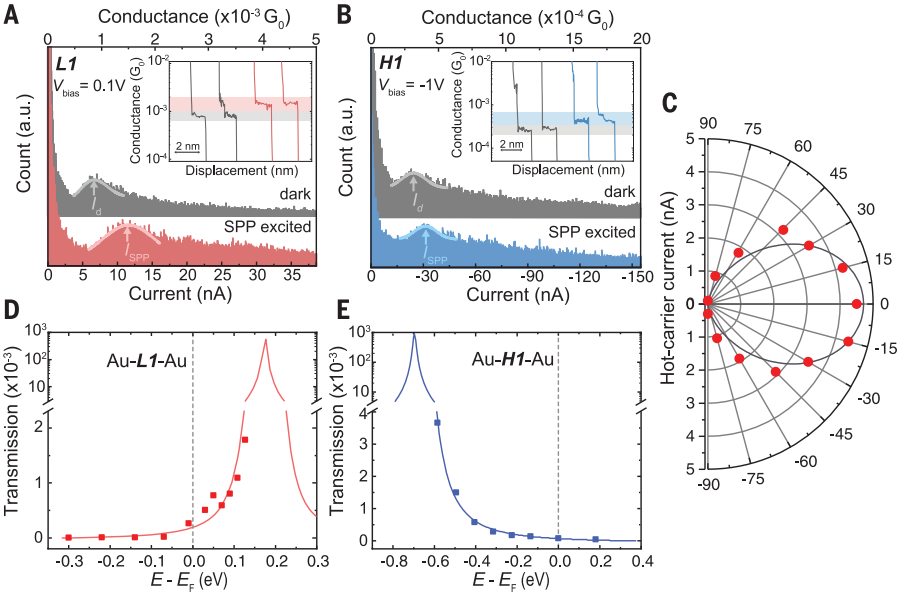

Fig. 2. Hot carrier–induced changes in SMJ currents, polarization dependence, and transmission characteristics of L1 and H1 molecules. (**A**) Current and conductance histograms of Au-**L1**-Au SMJs from more than 2000 traces of dark (gray) and SPP-excited (red) measurements at a V_{bias} of 0.1 V. Gaussian fits to the histogram peaks are represented as solid lines, and the vertical arrows indicate the most probable conductance and current. Inset shows representative conductance traces using the same color coding. (**B**) As in (A), but for Au-**H1**-Au junctions and a −1.0 V bias voltage. The gray and blue colors correspond to measurements from dark and SPP-excited cases, respectively. (**C**) Polarization dependence of the hot-carrier current for Au-**L1**-Au junctions (red circles) at 0.1 V bias voltage along with the best-fit $\cos^2\theta$ dependence (black line). (**D** and **E**) Measured transmission functions (note the linear and logarithmic scales) of Au-**L1**-Au and Au-**H1**-Au junctions along with the Lorentzian fits (solid lines).

Au-**L1**-Au junction (Fig. 2A) under the absence of plasmonic excitation [$G_0 \approx (12.9\ \text{kilohms})^{-1}$ is the quantum of electrical conductance], in good agreement with prior work (*22*). Subsequently, we illuminated the gratings with a focused 830-nm linearly polarized laser beam (0.3 mW/μm^2 power density) perpendicular to the grating strips, launching SPPs in the Au film (Fig. 1A). Concurrently, we measured the electrical current and found that the most probable current I_{SPP} is larger than I_d (Fig. 2A). We then determined the hot-carrier current as $I_{hot}(V_{bias} = 0.1\ \text{V}) = I_{SPP}(V_{bias} = 0.1\ \text{V}) - I_d(V_{bias} = 0.1\ \text{V})$. The measured $I_{hot}(V_{bias} = 0.1\ \text{V})$ displayed a strong dependence on the laser polarization (Fig. 2C), consistent with the polarization-dependent SPP excitation efficiency, indicating that the measured I_{hot} is due to the excitation of SPPs. Additional control experiments further confirmed that the measured I_{hot} is indeed due to hot-carrier effects and not because of an increased temperature or simple light-assisted transport [(*20*), section 6].

Next, we performed additional measurements from Au-**L1**-Au SMJs at the same location while varying V_{bias} from {−0.3 V:0.3 V}. The measured bias-dependent $I_{hot}(V_{bias})$ (fig. S16A) displayed an asymmetric shape with a peak around 0.15 V. Further, the transmission characteristics of Au-**L1**-Au junctions, necessary

for determining the spectral distribution of hot carriers (see Eqs. 1 and 2), were obtained using an experimental approach developed in (*23*) [(*20*), section 7]. Figure 2D shows the $T(E)$ obtained for Au-**L1**-Au junctions. Consistent with past work (*23*), we fit the measured $T(E)$ with a Lorentzian and obtained the energy of the peak to be $E_0 \approx 0.18$ eV relative to the Fermi energy (E_F) with a peak width of 2.6 meV (Fig. 2D), confirming the sharp nature of the peak [(*20*), section 7], in good agreement with past computational work (*22*). Subsequently, we determined $f_{hot}(E)$ from the measured $I_{hot}(V_{bias})$ and $T(E)$ of **L1** using Eq. 2. The measured $f_{hot}(E)$ (see Fig. 3A) revealed the relative hot-electron energy distribution (HEED), displaying a peak around 100 meV followed by a decaying tail extending up to about 330 meV above E_F. As the transmission function peak enters the window between the quasi-Fermi levels of the two contacts (E_F, $E_F - eV_{bias}$), extremely large currents flow through the molecular junction making the junction unstable and limiting the V_{bias} sweep window to {−0.3 V:0.3 V} and the energy window to {0.03 eV:0.33 eV} with respect to E_F [(*20*), section 7]. However, this is not a fundamental limitation, as additional measurements and analysis with Au-**L2**-Au SMJs enabled measurements of the HEED at higher energies, which revealed that there are negligibly few hot electrons with energies beyond 0.4 eV (dashed line in the inset of Fig. 3A) [(*20*), section 10].

To determine the hot-hole energy distribution (HHED), i.e., energies below E_F, we repeated measurements of $I_{hot}(V_{bias})$ in Au-**H1**-Au SMJs for V_{bias} in the range of {−1.5 V:1 V} (fig. S16B). Unlike for **L1**, where large $I_{hot}(V_{bias})$ was observed for positive V_{bias}, no perceptible $I_{hot}(V_{bias})$ was recorded in **H1** junctions for positive V_{bias}. Instead, $I_{hot}(V_{bias})$ in **H1** junctions increased above the noise floor for V_{bias} below −0.6 V and peaked around −1.2 V. Next, we measured the transmission characteristics of Au-**H1**-Au junctions and obtained the Lorentzian-shaped transmission characteristics shown in Fig. 2E, which features a peak at $E_0 \approx -0.7$ eV and a peak width of 6.8 meV, in good agreement with prior work (*23*). From the measured $T(E)$ and $I_{hot}(V_{bias})$, we obtained $f_{hot}(E)$ using Eq. 2 over the energy range {−1.2 eV:0.05 eV} (Fig. 3B). The HHED featured a peak around −0.1 eV and a decaying tail that extends to energies about −0.4 eV with respect to E_F.

To gain insights into the microscopic origin of our observations, we performed first-principle density functional theory (DFT) calculations (*11*) to compute the hot-carrier generation rates and subsequently used the Boltzmann transport equation under the relaxation time approximation (*25*) to obtain the steady-state HCEDs [(*20*), section 11]. For our calculations, we considered a geometry consisting of a Au film surrounded by a symmetric dielectric environment with a refractive index $n = 1.45$, mimicking the geometry in our experiments, which is known to support two plasmonic modes: a symmetric mode and an antisymmetric mode with distinct dispersion relations (*26*–*28*).

The computed HCEDs arising from the symmetric plasmonic mode on a 6-nm-thick Au film, obtained using both an energy-dependent electron-electron collision rate from Landau's Fermi liquid theory (FLT) (*29*) and an energy-independent scattering rate, are shown in Fig. 4A. Additionally, electron-phonon scattering is included via an energy-independent relaxation rate (*30*). These computational results are multiplied by a scaling factor so that the peak value is 1. The results obtained following FLT predict that hot carriers are largely populated within the energy window of {−0.4 V:0.4 V} relative to E_F, in excellent agreement with our experiments. In contrast, an energy-independent scattering rate results in hot carriers in a larger range of energies (Fig. 4A, blue curve) that disagree with our experimental observations. These findings establish the validity of using the energy-dependent electron-electron collision rate for modeling hot carriers in plasmonic nanostructures.

To understand the effect of film thickness, we measured the HCED in thicker (13-nm-thick) Au films. The measured HCED (Fig. 3, C and D) showed that the hot carriers are mostly populated around E_F. Further, the total number of hot carriers $\left[\int_{E_F-\hbar\omega}^{E_F+\hbar\omega} |f_{hot}(E)|dE\right]$ was found to be ~40% smaller than those measured on 6-nm-thick film. The observed reduction in the magnitude of HCED in thicker films can be attributed to the effect of surface-assisted absorption, that is, to the Landau damping (*13*, *15*, *25*) [see relevant discussion in (*20*), section 11]. To quantify the role of Landau damping, we computed the HCED in a 13-nm-thick film arising from the symmetric plasmonic mode, and electron-electron scattering rates from FLT (Fig. 4A), which revealed that the generated hot carriers are populated close to E_F, similar

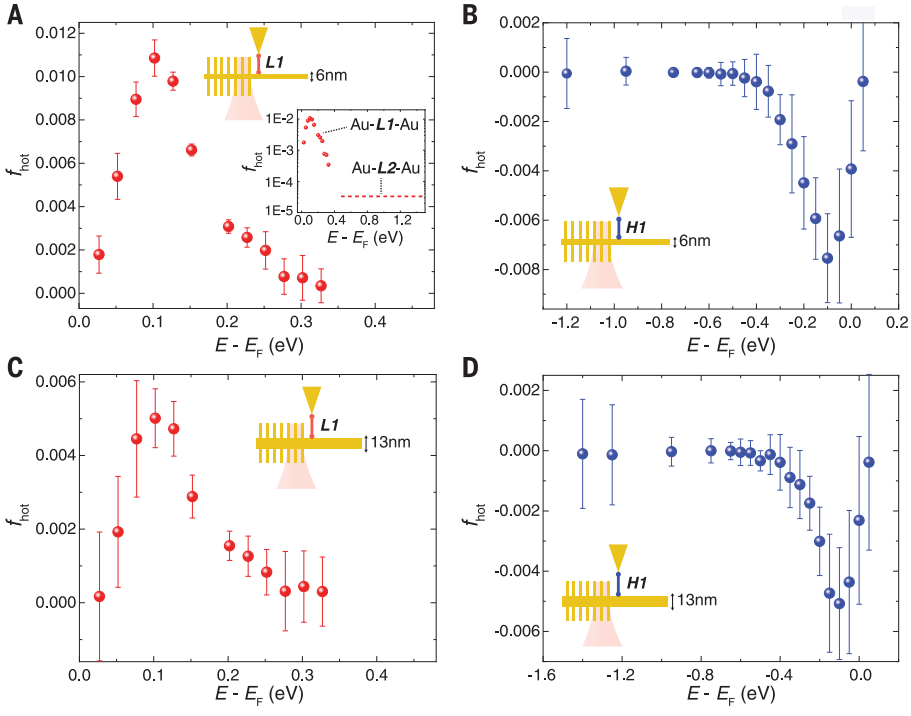

Fig. 3. Energy distributions of hot carriers in 6-nm-thick and 13-nm-thick Au films. (**A**) The measured hot-electron energy distribution (HEED) in a 6-nm-thick Au film obtained from measurements on Au-**L1**-Au and Au-**L2**-Au SMJs. The energy distribution in the range up to 0.33 eV was measured with Au-**L1**-Au junctions. The inset shows the HEED on a log scale, and the dashed line represents the upper bound on the average $f_{hot}(E)$ in the energy window {0.4 eV:1.45 eV}, as determined with Au-**L2**-Au junctions. (**B**) The measured hot-hole energy distribution (HHED) in a 6-nm-thick Au film using Au-**H1**-Au junctions under otherwise identical conditions compared with (A). (**C** and **D**) As in (A) and (B), but for measured hot-carrier energy distributions in a 13-nm-thick Au film. The error bars correspond to the propagated errors from uncertainties in the measured $I_{hot}(V_{bias})$.

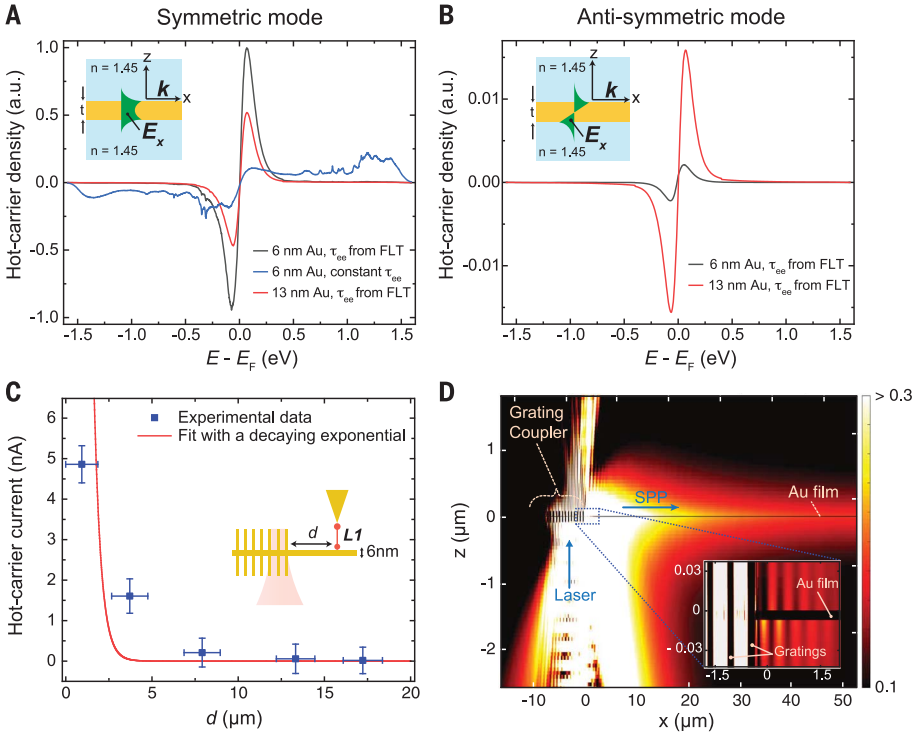

Fig. 4. Computed HCEDs, distance dependence, and intensity profile. (**A**) Computed HCEDs in 6-nm-thick and 13-nm-thick Au films, arising from the symmetric plasmonic mode with electron-electron scattering rates from either FLT or an energy-independent scattering rate and a constant electron-phonon relaxation rate. Inset shows the employed geometry and mode profile. a.u., arbitrary units; τ_{ee}, electron-electron relaxation time constant. (**B**) As in (A), but for the antisymmetric plasmonic mode. Note that the *y*-axis scale is smaller in (B) than in (A). (**C**) Measured I_{hot} through Au-**L1**-Au SMJs (V_{bias} = 0.1 V) for varying separations *d* between the probe tip and the grating edge. Error bars represent uncertainties in *d* and I_{hot}. The red curve is an exponential fit constrained to have a decay length of 405 nm, corresponding to the symmetric mode's decay constant in 6-nm-thick gold film [(*20*), section 14]. (**D**) Simulated intensity profile normalized to the incident field intensity upon illuminating the gratings with a focused 830-nm laser (spot size: 5.6 μm). Inset shows the intensity profile near the grating edge. The color map of the inset is adjusted to show the beating pattern and is different from the main panel color map.

to the 6-nm-thick film. However, about 43% fewer hot carriers are generated in the 13-nm-thick film, in good agreement with our experiments.

To elucidate the distance-dependence of hot-carrier generation, we measured I_{hot} for Au-**L1**-Au SMJs at a V_{bias} of 0.1 V for varying separations (*d*) from the grating edge on a 6-nm-thick gold film [see Fig. 4C and (*20*), section 14]. The measured I_{hot} decreases as the separation from the edge of the gratings increases and drops close to zero for $d > 7.5$ μm. To understand the observed distance dependence, we simulated [using the Lumerical finite-difference time-domain (FDTD) package] the intensity profile in the 6-nm-thick film upon illuminating the grating coupler with an 830-nm laser. A beating profile was observed close to the gratings (Fig. 4D), which we attribute to the interference between the two plasmonic modes [(*20*), section 13, and Fig. 4D, inset]. However, for $d > 10$ μm, the symmetric mode decays while the antisymmetric mode shows very little decay. Because there are no observed hot carriers at large separations, despite the presence of the antisymmetric mode, we conclude that the contribution of the antisymmetric mode to hot-carrier generation is negligible. Additional calculations (Fig. 4B) confirmed that the antisymmetric mode is indeed much less effective in generating hot electrons, resulting in only 0.25% (3.3%) hot carriers, in comparison to the symmetric mode for the 6-nm-thick (13-nm-thick) film.

Our scanning probe–based approach combines single-molecule quantum transport measurements and nanoplasmonics to directly map the steady-state energy distributions of hot carriers. The approaches developed will enable fundamental insights into hot-carrier generation processes and are critical for future hot carrier–assisted technologies.

REFERENCES AND NOTES

1. J. M. Ziman, *Principles of the Theory of Solids* (Cambridge Univ. Press, ed. 2, 1972).
2. S. Linic, P. Christopher, D. B. Ingram, *Nat. Mater.* **10**, 911–921 (2011).
3. S. Linic, U. Aslam, C. Boerigter, M. Morabito, *Nat. Mater.* **14**, 567–576 (2015).
4. L. Zhou *et al.*, *Science* **362**, 69–72 (2018).
5. A. Naldoni *et al.*, *Nanophotonics* **5**, 112–133 (2016).
6. C. Clavero, *Nat. Photonics* **8**, 95–103 (2014).
7. M. W. Knight, H. Sobhani, P. Nordlander, N. J. Halas, *Science* **332**, 702–704 (2011).
8. H. Chalabi, D. Schoen, M. L. Brongersma, *Nano Lett.* **14**, 1374–1380 (2014).
9. A. Sobhani *et al.*, *Nat. Commun.* **4**, 1643 (2013).
10. A. O. Govorov, H. Zhang, Y. K. Gun'ko, *J. Phys. Chem. C* **117**, 16616–16631 (2013).
11. R. Sundararaman, P. Narang, A. S. Jermyn, W. A. Goddard III, H. A. Atwater, *Nat. Commun.* **5**, 5788 (2014).
12. A. Manjavacas, J. G. Liu, V. Kulkarni, P. Nordlander, *ACS Nano* **8**, 7630–7638 (2014).
13. H. Zhang, A. O. Govorov, *J. Phys. Chem. C* **118**, 7606–7614 (2014).
14. T. Heilpern *et al.*, *Nat. Commun.* **9**, 1853 (2018).
15. J. B. Khurgin, *Faraday Discuss.* **214**, 35–58 (2019).
16. Y. Dubi, Y. Sivan, *Light Sci. Appl.* **8**, 89 (2019).
17. B. Xu, N. J. Tao, *Science* **301**, 1221–1223 (2003).
18. P. Reddy, S.-Y. Jang, R. A. Segalman, A. Majumdar, *Science* **315**, 1568–1571 (2007).
19. L. Cui *et al.*, *Science* **355**, 1192–1195 (2017).
20. See supplementary materials.
21. A. Vezzoli *et al.*, *Nanoscale* **7**, 18949–18955 (2015).
22. K. Wang *et al.*, *Chem. Sci.* **10**, 2396–2403 (2019).
23. B. Capozzi *et al.*, *Nano Lett.* **16**, 3949–3954 (2016).
24. W. Lee *et al.*, *Nature* **498**, 209–212 (2013).
25. L. V. Besteiro, X. T. Kong, Z. Wang, G. Hartland, A. O. Govorov, *ACS Photonics* **4**, 2759–2781 (2017).
26. S. Bozhevolnyi, *Plasmonic Nanoguides and Circuits* (Pan Stanford Publishing, 2009).
27. P. Berini, *Adv. Opt. Photonics* **1**, 484–588 (2009).
28. A. V. Zayats, S. A. Maier, *Active Plasmonics and Tuneable Plasmonic Metamaterials* (Wiley, 2013).
29. P. Coleman, *Introduction to Many-Body Physics* (Cambridge Univ. Press, 2015).
30. R. H. M. Groeneveld, R. Sprik, A. Lagendijk, *Phys. Rev. B* **51**, 11433–11445 (1995).

ACKNOWLEDGMENTS

The authors acknowledge fruitful discussions with P. Nordlander, S. Datta, and R. Sundararaman. **Funding:** The work was supported by a grant from the Army Research Office [grant W911NF-19-1-0279 to P.R., V.M.S., and E.M. (design of plasmonic structures and modeling)]. P.R. and E.M. acknowledge support from the Department of Energy [DOE-BES award DE-SC0004871 (scanning probe measurements and analysis)], the U.S. Office of Naval Research [ONR award N00014-16-1-2672 (synthesis of **H1**)], and the U.S. National Science Foundation, award 1803983). V.G., P.R., and E.M. thank the Department of Mechanical Engineering at the University of Michigan for support via a RIP-ME grant (DFT calculations). A.B. and V.M.S. acknowledge support from the Air Force Office of Scientific Research grants FA9550-17-1-0243 and FA9550-20-1-0124 (realization of ultrathin gold films and surface plasmon structures). V.G. acknowledges the support of the Army Research Office for a DURIP award (grant W911NF1810242), which provided the computational resources for the DFT calculations. A.V. and S.J.H. acknowledge support from the EPSRC (grant EP/M029522/1). **Author contributions:** H.R., K.W., P.R., V.M.S., and E.M. conceived of the project. H.R. and K.W. designed and developed the experimental methods under the guidance of P.R., V.M.S., and E.M. H.R. fabricated the ultrathin gold plasmonic structures. K.W. and H.R. conducted the single-molecule transport measurements. Z.K. performed the FDTD field profile and thermal simulations under the guidance of A.B. L.Z. conducted the ab initio calculations on hot-carrier generation rates under the supervision of V.G. S.Y. prepared the template stripped gold films for transmission function mapping measurements. A.V. synthesized the LUMO molecule **L1** under the guidance of S.J.H. P.R., V.M.S., and E.M. supervised the project. H.R., K.W., L.Z., A.B., P.R., V.M.S., and E.M. wrote the manuscript with comments and inputs from all other authors. **Competing interests:** The authors declare no competing interests. **Data and materials availability:** All of the data pertaining to the work are available in the manuscript or the supplementary materials.

SUPPLEMENTARY MATERIALS

science.sciencemag.org/content/369/6502/423/suppl/DC1
Materials and Methods
Supplementary Text
Figs. S1 to S25
References (*31*–*54*)

23 February 2020; accepted 21 May 2020
Published online 4 June 2020
10.1126/science.abb3457

Determining plasmonic hot-carrier energy distributions via single-molecule transport measurements

Harsha Reddy, Kun Wang, Zhaxylyk Kudyshev, Linxiao Zhu, Shen Yan, Andrea Vezzoli, Simon J. Higgins, Vikram Gavini, Alexandra Boltasseva, Pramod Reddy, Vladimir M. Shalaev and Edgar Meyhofer

Science **369** (6502), 423-426.
DOI: 10.1126/science.abb3457originally published online June 4, 2020

Taking the temperature of hot carriers

Hot carriers are expected to arise in plasmonic nanostructures because of the nonradiative decay of surface plasmons. However, identifying and determining just how "hot" these carriers actually are has been challenging. Reddy *et al.* devised a technique that looks at the carrier transport through a single molecular junction, which effectively acts as an energy filter, and show that it can be used to determine the distribution of hot carriers in a plasmonic nanostructure (see the Perspective by Martín-Moreno). These hot carriers could be harnessed to enhance the performance of technologies, including plasmon-driven photochemistry, solar energy–harvesting devices, and efficient photodetectors.

Science, this issue p. 423; see also p. 375

Science (print ISSN 0036-8075; online ISSN 1095-9203) is published by the American Association for the Advancement of Science, 1200 New York Avenue NW, Washington, DC 20005. The title *Science* is a registered trademark of AAAS.